
Video as Natural Augmentation: Towards Unified AI-Generated Image and Video Detection

Zhengcen Li¹, Chenyang Jiang¹, Liangxu Su¹, Tong Shao¹, Shiyang Zhou^{1,3}
Ming Tao², Jingyong Su¹

¹ Harbin Institute of Technology, Shenzhen

² Pengcheng Laboratory

³ Shenzhen Loop Area Institute

lizhengcen@stu.hit.edu.cn, sujingyong@hit.edu.cn

Abstract

AI-generated content (AIGC) is rapidly improving, creating an urgent need for detectors that generalize across data sources, deployment pipelines, and visual modalities. A strongly generalizable detector should remain robust under distributional variations. However, we identify a consistent failure mode: SOTA AI-generated image detectors often collapse when applied to frames extracted from videos. Through systematic analysis, we show that this cross-modal gap arises from both entangled *synthesis-agnostic* video processing shifts, including color conversion, codec compression, resizing, and blur, and *model-specific* fingerprints introduced by modern video generators. Motivated by these findings, we propose **VINA** (Video as Natural Augmentation), a unified AIGC detection framework that jointly trains on image and video data. VINA uses video frames as physically grounded natural augmentations and further introduces a cross-modal supervised contrastive objective to align image and video representations under a shared real/fake decision boundary. Extensive experiments on 14 image, video, and in-the-wild benchmarks show that VINA delivers bidirectional gains, improves robustness and transferability, and achieves state-of-the-art performance across nearly all evaluated settings without complex augmentation or dataset-specific tuning.

1 Introduction

Recent advances in AI-generated content (AIGC) have enabled diffusion models and large-scale transformers to produce highly realistic and semantically consistent images [1] and videos [2]. As generation quality improves, synthetic media increasingly blurs the boundary between authentic and generated content, lowering the cost of creating persuasive misinformation at scale and weakening public trust [3]. The broad availability of both image and video generation models and products therefore creates an urgent demand for accurate, robust, and broadly generalizable detectors that can operate reliably in diverse real-world settings.

Generalization is the central challenge in AIGC detection. A practical detector must transfer across generators, data sources, and deployment pipelines, especially to in-the-wild media whose provenance and post-processing history are unknown. Existing AI-generated image (AIGI) detectors mainly exploit local pixel artifacts [4], frequency-domain traces [5], reconstruction behavior [6], or high-level semantics [7, 8]. Recent work further improves generalization through data alignment [9], where diffusion or VAE models inject controlled synthetic traces into real images at the pixel [10] or frequency level [11]. Although these methods improve cross-generator and cross-dataset transfer, their performance still deteriorates under unseen generators [12], real-world online samples [13],

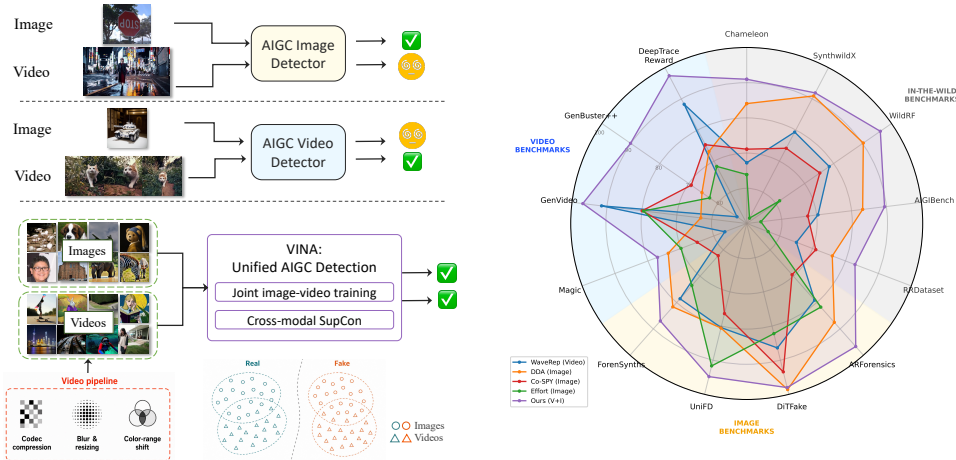


Figure 1: **Motivation and benchmark performance of unified AIGC detection.** **Left:** Asymmetric cross-modal failures motivate VINA to learn from both image and video data. **Right:** Average accuracy across image, video, and in-the-wild AIGC benchmarks shows that image-based detectors degrade sharply on videos, while joint training improves cross-modal generalization.

and media subjected to heavy compression or platform degradation [14]. This indicates that current detectors remain vulnerable to shortcut cues and distribution shifts that are not tied to synthesis itself.

In this paper, we identify a novel systematic failure mode: state-of-the-art AIGI detectors collapse when evaluated on video frames. As summarized in the left and right panels of Figure 1, image-trained detectors that perform competitively on image benchmarks often drop sharply on AI-generated video (AIGV) benchmarks, with several methods approaching random guessing. This failure persists even for recent detectors designed for stronger cross-generator transfer, showing that the problem is not merely a matter of unseen generators. Meanwhile, dedicated AIGV detectors [15–17] remain relatively underexplored and often fail to preserve strong image-domain generalization. In practice, a AIGC detector cannot assume its input is a clean image; it may receive a frame extracted from a compressed video or an image after online platform degradation. These observations suggest that treating AIGI and AIGV detection as separate tasks leaves a fundamental cross-modal generalization gap.

We analyze this failure from the properties of real video data. Video frames are not simply still images sampled from another generator distribution. They are produced by real acquisition, rendering, compression, and distribution pipelines. Compared with common image datasets, video frames contain stronger *synthesis-agnostic* shifts, including realistic imaging and motion blur, codec-induced frequency decay, limited-range color conversion, resizing, and repeated platform recompression. They also cover more diverse scenes and camera motions, while modern video generators introduce additional model-specific fingerprints related to temporal modules and motion synthesis. These factors suppress high-frequency micro-artifacts that image detectors often exploit as shortcuts, while introducing low- and mid-frequency statistics that are underrepresented in image-only training. We therefore view video frames as physically grounded natural augmentations: they expose detectors to realistic degradations that are difficult to reproduce with handcrafted JPEG, blur, or color perturbations.

To address this gap, we propose **VINA (VIdeo as Natural Augmentation)**, a joint video–image training framework for unified AIGC detection. VINA augments existing image training sets [18, 19, 9] with AIGV detection data [15, 20] and trains a single detector for both image and video inputs. Beyond binary supervision on mixed batches, we introduce a cross-modal supervised contrastive (CM-SupCon) loss that aligns image and video features with the same real/fake label while preserving the decision boundary. This regularizes the unified representation space, reduces reliance on modality- or source-specific shortcuts, and encourages the detector to use generative traces that remain discriminative across both clean images and degraded video frames. Extensive experiments show bidirectional gains: joint training substantially improves video detection while also improving image and in-the-wild performance. Without complex augmentation, explicit alignment, or dataset-specific tuning, VINA

achieves strong state-of-the-art results across multiple backbones and data-source combinations, reaching 90.4% average accuracy on video benchmarks, 94.1% on image benchmarks, and 92.9% on in-the-wild benchmarks. Our contributions are summarized as follows.

1. We reveal that state-of-the-art AIGI detectors systematically fail on video benchmarks, formulate unified AIGC detection as a generalization problem, and show that training and evaluation should jointly cover AI-generated images and videos rather than treating them as isolated tasks.
2. We propose VINA, a joint video–image training framework with a CM-SupCon objective that regularizes image and video representations under a unified decision boundary, suppressing source- and modality-specific shortcut cues.
3. Extensive experiments across 14 image, video, and in-the-wild benchmarks show that VINA brings bidirectional gains for both videos and images, substantially improves in-the-wild robustness, and generalizes across multiple backbones and data sources without complex augmentation, explicit alignment, or dataset-specific tuning.

2 Related Work

2.1 Generative Models

Image Generative Models. Image generation has evolved from GAN-based models [21] to VAE/VQ-VAE frameworks [22, 23] and diffusion models [24]. Latent Diffusion Models (LDMs) [25] improve efficiency by denoising in a compressed latent space, while recent Diffusion Transformers (DiTs) [26], autoregressive models [27] and unified models [28] further improve scalability with transformer-based architectures.

Video Generative Models. Video generation extends image generation to the spatiotemporal domain. Early systems such as Make-A-Video [29] and Stable Video Diffusion [30] adapt image diffusion backbones with temporal modeling. Recent representative systems, including Sora [2], Wan [31], Kling [32], and Seedance [33], increasingly rely on video diffusion transformers, multimodal conditioning, and large-scale pretraining and post-training to improve visual fidelity, motion consistency, and controllability.

Different generative architectures often leave distinct generative traces. To ensure systematic evaluation across modalities, we assemble a comprehensive detection benchmark that spans the major image and video architectures, including GAN, LDM, DiT, autoregressive models, as well as challenging in-the-wild samples.

2.2 AIGC Detection

AI-Generated Image Detection. Significant research has focused on developing generalizable methods for detecting synthetic images [18, 7]. These include approaches based on spectral artifacts [5], reconstruction error [34–36], pixel-level features [4, 6], and the adaptation of visual backbones [37, 38, 8, 39]. Typically trained on images from specific generative models [40, 19], these methods aim to achieve generalization across both different models and architectures.

AI-Generated Video Detection. Early methods for detecting AI-generated videos (AIGVs) primarily targeted facial manipulations or biological inconsistencies. With the advent of high-fidelity video synthesis, the focus has shifted toward detecting fully AI-generated scenes [41]. This progress is supported by million-scale benchmarks such as GenVideo [15] and GenVidBench [42], which evaluate cross-generator generalization. Physics-driven methods like D3 [43] and NSG-VD [16] identify synthetic content by quantifying deviations from Newtonian mechanics or violations of probability flow conservation in the spatiotemporal latent space. Recent video-based methods [20, 44–46] or unified methods [47–49] use multimodal large language models to provide human-interpretable reasoning and artifact localization, but they remain limited by LLM hallucination and high computational cost; moreover, their vision encoders are primarily optimized for high-level semantic perception and may be insufficiently sensitive to subtle artifacts [50].

Dataset Alignment. Relying exclusively on frequency-domain cues or on training data tied to a specific generative model can introduce vulnerability to dataset bias [9], thereby limiting generalization. To address this, recent works employ generative models such as diffusion models [35] or VAEs [51, 52] to inject controlled artifact patterns, either in pixel space [10] or in the frequency domain [11]. By strictly isolating these injected artifacts from other confounding factors, such datasets facilitate the training of more robust and generalizable detection models.

However, existing methods are typically confined to a single task, focusing either on image or video detection, and do not account for the intrinsic differences between still images and video frames. In contrast, we explicitly unify these two tasks within a single training framework to enhance the generalization capability of visual AIGC detection.

3 Method

3.1 Motivation and Analysis

Why do AIGI detectors fail on video frames? Despite semantic similarities between generated images and video frames, our empirical observations in the right panel of fig. 1 reveal a significant performance drop when state-of-the-art AI-generated image (AIGI) detectors are applied to video frames. To understand the root causes of this generalization gap, we analyze the domain shift from two perspectives: *synthesis-agnostic* degradation from the video processing pipeline, and *model-specific* fingerprints intrinsic to video generation architectures. We conduct a qualitative analysis to examine the potential distribution gap between image and video data. Specifically, we randomly sample data from existing real-world datasets [53] and AIGC-generated sources [19, 54] for both modalities.

Compression Artifacts. Quantization noise in videos differs fundamentally from that in still images. As shown in Figure 2, DCT AC coefficients from video frames display a smoother distribution, with substantially more zeros and a sharper peak near zero compared to JPEG images. This indicates more refined and often more aggressive quantization, driven by inter-frame prediction, variable block sizes, and adaptive quantization. Videos also frequently undergo recompression during distribution, making their DCT distributions even steeper after additional JPEG compression. These distinct frequency-domain statistics can mislead detectors that rely on local pixel cues [13] or frequency features [5].

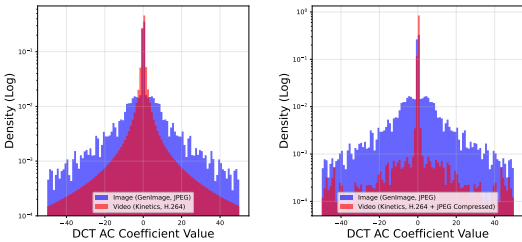


Figure 2: **DCT AC coefficient distributions.** H.264 and recompressed video frames exhibit sharper near-zero peaks than original JPEG images.

Blur and Frequency Decay. Video frames are inherently prone to spectral degradation due to motion blur, aggressive compression, and resolution rescaling. As illustrated by the Radially Averaged Power Spectral Density (RAPSD) [55] plot in fig. 3, real videos exhibit the most pronounced high-frequency energy decay, suggesting that the video pipeline acts as a strong low-pass filter. The additional visualization in Section A (fig. 6) further shows that this filtering substantially reduces the spectral discrepancy between real and synthetic content in the video domain compared to the image domain, helping explain why AIGC detectors degrade under unseen video scenarios.

Color Space and Luminance Range. Figure 4 shows that pixel-intensity statistics shift markedly between images and videos. Most real-world videos use a limited (TV) luminance range (e.g., $Y \in [16, 235]$), which removes extreme values and can create empty histogram bins after integer rescaling. While standard augmentation can partially mitigate this discrepancy, detectors designed to capture color mismatches [56] are prone to fail on such out-of-distribution frames.

Model-Specific Fingerprints. Beyond pipeline artifacts that differentiate video frames from still images, video generation models introduce distinct, model-driven fingerprints [11, 57]. Due to temporal modules and specific motion simulation, video generative models often produce unnatural blur and motion-related artifacts, which can manifest as spatial warping or illogical textures in

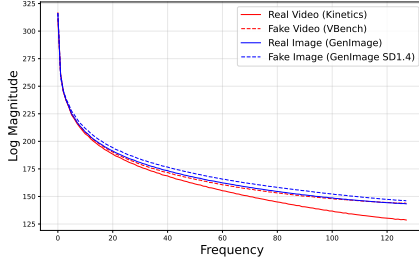


Figure 3: **RAPSD analysis of video and image datasets.** Real videos exhibit significant high-frequency decay, reflecting compression and motion blur.

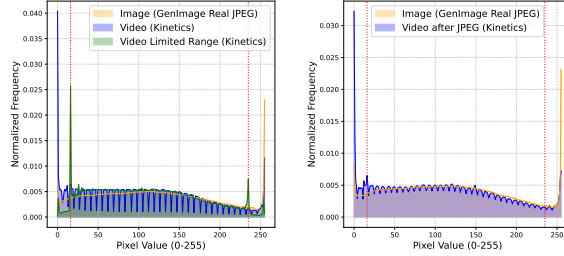


Figure 4: **Pixel luminance distributions.** We analyze 10k samples each from Kinetics (video) and GenImage (image). Video frames show shifted statistics before and after JPEG double compression.

individual frames [58]. The spectral visualization in Figure 6 shows that the noise spectrum of AI-generated videos differs noticeably from that of text-to-image-generated images, with additional model-specific patterns provided in fig. 7.

3.2 Consistency via Video-Image Joint Training

An ideal AIGC detector should ignore irrelevant pipeline-induced discrepancies and learn robust cues intrinsic to generative models. However, despite alignment efforts [9, 11], intrinsic domain shifts often cause detectors trained solely on images to fail on video frames. At the same time, videos provide rich natural variation that can regularize detectors beyond handcrafted augmentations. To bridge this gap, we propose a joint training paradigm that leverages video data for natural video-augmented consistency learning.

Formally, let \mathcal{D}_{img} be a dataset of static images and \mathcal{D}_{vid} be a dataset of video frames, both annotated with real/fake labels. We model video frames as image signals subjected to a complex, non-differentiable degradation function $\mathcal{T}(\cdot)$. If x represents a pristine visual signal, a video frame v is obtained via:

$$v = \mathcal{T}(x) = \text{Codec}(\text{Resize}(\text{MotionBlur}(x))) \quad (1)$$

Crucially, the transformation $\mathcal{T}(\cdot)$ introduces intricate temporal motion blur and sophisticated compression artifacts. These real-world video degradations are entangled and complex thus cannot be easily simulated by 2D data augmentations (e.g., Gaussian blur or JPEG re-compression). Consequently, standard detectors trained only on \mathcal{D}_{img} tend to latch onto high-frequency artifacts in x that are inevitably destroyed by the complex dynamics of $\mathcal{T}(\cdot)$. Joint training on image and video samples provides an implicit consistency constraint by exposing the classifier to both pristine and naturally degraded observations. However, relying only on binary supervision may still allow the feature space to remain modality-separated. Inspired by [59], we add an explicit cross-modal supervised contrastive regularizer that aligns image and video representations with the same real/fake label.

Let z_i denote the ℓ_2 -normalized feature of sample i in a mini-batch, with class label $y_i \in \{0, 1\}$ and modality label $m_i \in \{0, 1\}$ indicating image or video. For each anchor i , we define its positive set using only cross-modal samples with the same class label:

$$P(i) = \{j \neq i : y_j = y_i \wedge m_j \neq m_i\}. \quad (2)$$

The cross-modal supervised contrastive loss is then

$$\mathcal{L}_{\text{CM-SupCon}} = \frac{1}{|\mathcal{V}|} \sum_{i \in \mathcal{V}} \frac{-1}{|P(i)|} \sum_{p \in P(i)} \log \frac{\exp(z_i^\top z_p / \tau)}{\sum_{k \neq i} \exp(z_i^\top z_k / \tau)}, \quad (3)$$

where τ is the temperature and $\mathcal{V} = \{i : |P(i)| > 0\}$ denotes anchors with at least one valid cross-modal positive. This design differs from standard same-label contrastive learning: same-modality samples are not counted as positives, preventing the trivial solution in which image and video features cluster separately while sharing the same class label.

Our final objective combines binary classification with this explicit cross-modal feature constraint:

$$\mathcal{L} = \mathcal{L}_{\text{BCE}} + \lambda \mathcal{L}_{\text{CM-SupCon}}. \quad (4)$$

Table 1: **Comparison results on 8 established benchmarks in ACC(%), including 4 video-based and 4 image-based benchmarks.** Except for DeMamba, for which no public checkpoint is available and which we retrain on GenVideo-100k, all results are obtained by us using the officially released checkpoints and the corresponding inference-time transforms. Detailed results are provided in Section C.

Method	Type	Video					Image				ALL AVG	
		AVG	Magic	GenVideo	GenBuster++	DeepTraceReward	AVG	ForenSynths (GAN)	UniFD (LDM)	DiTFake		ARForensics
DeMamba [15] (100k)	Video	69.2	63.1	90.4	51.5	71.9	57.7	54.6	57.4	63.2	55.8	63.5
Qwen2.5-ViT [20]	Video	<u>85.0</u>	81.3	95.6	68.8	94.4	65.4	51.4	60.0	80.3	69.9	75.2
WaveRep [11]	Video	72.4	56.6	91.5	53.4	88.3	81.1	78.6	80.5	86.4	79.1	76.8
NPR [4]	Image	51.7	50.1	55.4	50.9	50.5	80.3	76.2	92.8	76.9	75.3	66.0
FatFormer [37]	Image	52.4	49.5	56.5	51.4	52.0	80.4	88.9	93.5	60.0	79.1	66.4
RINE [38]	Image	51.5	42.2	56.5	58.4	48.9	79.6	91.8	90.5	57.0	79.0	65.5
Effort [8]	Image	69.5	67.4	79.5	62.8	68.3	82.3	73.5	91.7	82.2	81.7	75.9
Co-Spy [6]	Image	72.4	65.0	79.9	69.2	75.3	75.4	62.2	76.4	93.4	69.4	73.9
Co-Spy (ProGAN)	Image	50.9	49.7	54.1	50.1	50.0	88.4	83.0	94.4	90.8	85.6	69.7
DDA [9]	Image	68.9	73.9	63.2	65.5	73.1	87.1	81.7	80.6	98.6	87.5	78.0
B-Free [10]	Image	70.6	71.6	80.8	58.3	71.9	91.2	88.2	89.1	95.5	91.9	80.9
VINA (Pika+ProGAN)	V+I	79.5	64.3	90.8	80.1	82.9	<u>92.0</u>	82.0	94.8	97.2	94.1	85.8
VINA (GenVideo+SD1.4)	V+I	82.9	72.0	95.7	71.2	92.7	91.8	88.9	94.5	95.1	88.5	87.4
VINA (140k+DDA)	V+I	90.4	77.1	96.9	90.1	97.4	94.1	87.0	94.8	98.0	96.7	92.3

Here, \mathcal{L}_{BCE} is computed over mixed image and video mini-batches. The CM-SupCon term explicitly pulls real-image features toward real-video features and fake-image features toward fake-video features, while the contrastive denominator preserves real/fake separation. As a result, the detector learns features that are both class-discriminative and less tied to modality-specific compression, blur, or color-range shortcuts.

4 Experiments

4.1 Experimental Setup

Training Datasets and Evaluation Benchmarks. We compare three video-image training combinations with different data sources: Pika-100k from GenVideo [15, 60] with ProGAN-4class [40], GenVideo-100k [15] with SD1.4 from GenImage [19], and the 140k video set from Qwen2.5-ViT [20] with DDA [9]. Our evaluation spans 14 diverse benchmarks: four AIGC video detection benchmarks (Magic Videos [20], GenVideo-val [15], Genbuster++ [47], DeepTraceReward [58]), five AIGC image detection benchmarks (Forensics [18], UniFD [7], DiTFake [5], ARForensics [36]), and five in-the-wild benchmarks (Chameleon [13], SynthWildX [61], WildRF [62], AIGIBench [63], RR-Dataset [14]). Table 9 provides a summary. For all benchmarks except GenVideo, we report mean accuracy (ACC) and average precision (AP) across subsets. Due to the severe class imbalance (far fewer fake than real samples) within GenVideo-Val’s subsets, we report its overall ACC and AP instead. Full results for each benchmark are provided in Section C.

Baselines. We compare our approach with the following baselines: video-based AIGC detectors: DeMamba [15], WaveRep [11], and Qwen2.5-ViT [20]; image-based AIGC detectors: NPR [4], FatFormer [37], RINE [38], Effort [8], Co-SPY [6], MIRROR [64]; as well as models trained on aligned datasets: B-Free [10], DDA [9]. For baselines with public checkpoints, we use the officially released checkpoints and preprocessing pipelines; for DeMamba, whose checkpoint is not publicly available, we retrain it on GenVideo-100k. Additional implementation details are provided in Section B.

Implementation Details. Unless otherwise specified, we use DINOv3-Large as the visual backbone and attach a single MLP classification layer, with all parameters tuned end-to-end. Images and video frames are processed at a fixed resolution of 256×256 . To handle diverse aspect ratios, each input is resized with its original aspect ratio preserved until the shorter side reaches 256 pixels, followed by a 256×256 crop. During training, we sample one frame per video clip, apply random frame sampling and random cropping, and use only random horizontal flipping as additional augmentation. During

Table 2: **Benchmarking results on in-the-wild benchmarks in terms of balanced ACC(%)**. † indicates that the results are obtained from their papers.

Method	Chame	SynthWildx [61]			WildRF [62]			AIGIBench [63]		RR-Da	AVG
	-leon [13]	DALLE3	Firefly	Midj.	FB	Reddit	Twitter	SocRF	ComAI	taset [14]	
WaveRep [11]	67.9	72.9	94.9	70.2	75.3	77.3	82.9	68.6	72.2	65.1	74.7
NPR [4]	53.1	40.6	63.5	46.5	74.1	63.8	48.5	53.3	55.1	60.9	55.9
FatFormer [37]	51.1	47.4	59.7	49.8	54.4	69.5	42.5	56.9	51.9	53.0	53.8
RINE [38]	70.0	45.7	68.6	48.0	52.5	67.8	45.8	56.0	51.2	52.1	55.8
Effort [8]	65.4	51.6	55.7	47.9	57.8	58.3	67.9	51.4	56.8	56.5	56.9
CO-SPY [6]	78.4	72.0	79.7	70.8	73.1	77.3	75.3	68.2	66.7	71.0	73.3
DDA [9]	82.4	92.4	87.2	93.1	93.1	86.4	91.2	81.7	84.6	76.0	86.8
B-Free [10]	76.6	95.7	95.8	95.6	95.3	86.5	97.9	85.2	81.5	72.3	88.2
MIRROR† [64]	90.7	95.9	88.4	94.9	97.1	96.6	96.4	87.6	93.4	78.9	<u>92.0</u>
VINA (Pika+ProGAN)	86.8	75.9	76.6	75.7	87.2	83.7	91.2	74.2	89.9	67.4	80.9
VINA (GenVideo+SD1.4)	88.7	93.1	89.2	94.1	96.9	95.5	96.7	90.9	91.5	77.5	91.4
VINA (140k+DDA)	91.4	94.5	89.2	94.7	96.6	96.7	98.1	90.9	93.9	82.7	92.9

inference, we select the middle frame of each video and apply center cropping. We deliberately avoid extra data augmentation or JPEG alignment to isolate the effect of video-image joint training. Models are trained with AdamW for 10 epochs using a fixed learning rate of 1×10^{-6} , a batch size of 64, and early stopping based on validation loss. The supervised contrastive term uses $\lambda = 0.05$ in the final objective, with a temperature $\tau = 0.07$ in the CM-SupCon loss. All reported results are produced by a single model without dataset-specific parameter tuning.

4.2 Cross-Dataset Evaluation

Compared to Video-based and Image-based Detectors. As indicated in table 1, *video-based detectors* exhibit asymmetric generalization. Qwen2.5-ViT [20] performs strongly on video benchmarks but degrades on images, while DeMamba [15] shows limited transfer across both modalities when retrained on GenVideo-100k. WaveRep [11] fine-tunes a DINOv2 image backbone on video data, preserving better image generalization but yielding weaker video performance. In contrast, our jointly trained detector reaches 90.4% average ACC on video benchmarks using only one frame at inference. Moreover, *image-based detectors* show a pronounced cross-modal failure. Early methods such as NPR [4], FatFormer [37], and RINE [38] perform well on several image benchmarks but often collapse on videos. More recent detectors trained with aligned datasets, such as DDA [9] and B-Free [10], improve cross-dataset generalization but still suffer substantial video-domain degradation. Our method consistently outperforms these image-only detectors on both image and video benchmarks, demonstrating stronger cross-modal robustness.

Joint Video-Image Training. To isolate the effect of video data, we deliberately avoid complex augmentation and high-resolution processing widely applied in image-based methods [9, 10]; nevertheless, the proposed strategy already achieves state-of-the-art performance. Our method uses video frames as natural augmentations and consistency regularizers, and its gains are not tied to a specific source: both early combinations such as Pika+ProGAN and higher-quality mixtures such as 140k+DDA substantially outperform single-modality baselines, with more detailed evidence in Table 4. Moreover, our approach is complementary to explicit alignment, augmentation, and post-processing techniques, which can be combined with joint training to further raise the performance ceiling.

4.3 Comparison on In-the-Wild Benchmarks

In-the-wild benchmarks better reflect real deployment scenarios, where samples may come from unknown generators, undergo unknown post-processing, and be further compressed or degraded by online platforms. As shown in Table 2, early image detectors such as NPR [4], FatFormer [37], and RINE [38] largely fail under these conditions, indicating limited generalization and strong reliance on shortcut cues. Methods trained with aligned datasets or strong augmentations, such as DDA [9], B-Free [10], and WaveRep [11], achieve better overall robustness, but still show clear weaknesses on challenging benchmarks such as Chameleon and RR-Dataset. Our method remains competitive with and often outperforms these methods, including MIRROR [64], which also uses a DINOv3 backbone. These results show that joint video-image training provides strong in-the-wild generalization without

Table 3: **Ablation Study (ACC) on Joint Video-Image Training using Different Vi-Training with Different Data Sources (ACC).** Backbone SD1.4), V=Video Dataset (140k).

Backbone	Training Data	Video AVG	Image AVG	Chameleon	Mean ACC
CLIP ViT-L [65]	I	51.6	70.5	57.9	60.0
	V	87.4	63.3	43.8	64.8
	V+I	88.0	84.8	84.7	85.7
DINOv2 ViT-L [66]	I	59.5	66.8	58.2	61.5
	V	88.8	70.2	46.6	68.6
	V+I	89.2	86.3	84.0	86.5
DINOv3 ViT-L [67]	I	59.6	75.1	59.5	64.7
	V	88.7	79.8	49.5	72.7
	V+I	89.1	88.4	89.0	88.8

Table 5: **Ablations on Strategies for Bridging the Image-Video Gap.** We compare data augmentations designed for format adaptation with our proposed Joint training approach.

Method	Video AVG	Image AVG	Chameleon	Mean ACC
DINOv3 (trained on DDA)	68.4	89.8	78.7	78.9
+ random color jitter	68.5	91.0	81.3	80.3
+ random chain degradation	71.5	88.8	85.4	81.9
+ random HEIF compression	73.5	88.9	85.5	82.6
+ random WebP compression	72.4	89.8	88.9	83.7
DINOv3 (DDA+140k)	89.8	92.9	90.4	<u>90.9</u>
+ CM-SupCon loss (Ours)	90.4	94.1	91.4	92.0

Table 6: **Image Performance Comparison after JPEG Compression (Q=96).**

Method	JPEG	Image ACC	Image AP
SAFE [5]	✓	94.8	96.6
		50.2	52.0
CO-SPY [6]	✓	88.4	94.0
		53.1	54.6
Effort [8]	✓	82.3	89.1
		67.5	77.0
VINA	✓	87.3	97.2
		86.3	97.1

relying on a specific data source or complex alignment and augmentation pipelines, underscoring both the necessity of unified AIGC detection and the effectiveness of our approach.

4.4 Ablation Study

We conduct ablations to examine three factors behind the proposed joint training strategy: whether the gain is consistent across vision backbones, whether it depends on particular image or video data sources, and whether synthetic degradation strategies can bridge the same video-image gap.

Ablation Study on Model Backbone. As shown in Table 3, joint image-video (I+V) training is consistently effective across CLIP, DINOv2, and DINOv3 backbones. More importantly, the gains are bidirectional. Image-only training performs poorly on videos, while video-only training improves video accuracy but substantially hurts image and Chameleon performance. Combining both modalities resolves this trade-off: adding video data greatly improves video robustness, and adding image data restores strong image and in-the-wild generalization. This demonstrates that the benefit comes from complementary cross-modal supervision rather than a particular backbone.

Ablation Study on Data Sources. Table 4 further shows that the proposed strategy is not tied to a specific data source. Different image-video combinations all achieve strong performance, whereas simply scaling up image-only data (DDA+SD1.4 or DDA+SD1.4+ProGAN) or video-only data (140k+GenVideo) does not improve generalization and can even degrade the mean accuracy. In contrast, joint training achieves substantially stronger results with smaller data mixtures, indicating that the gain comes from the joint image-video training itself rather than from increased data scale or carefully selected sources.

Ablation Study on Video-Image Gap Bridge Strategy. Motivated by the analysis in section 3.1, we compare several synthetic degradation strategies that approximate video-domain shifts, including color jitter, HEIF/WebP compression, and a random degradation chain. As shown in Table 5, these augmentations moderately improve video and in-the-wild performance, confirming that compression and color-space shifts contribute to the image-video gap. However, their gains remain much smaller

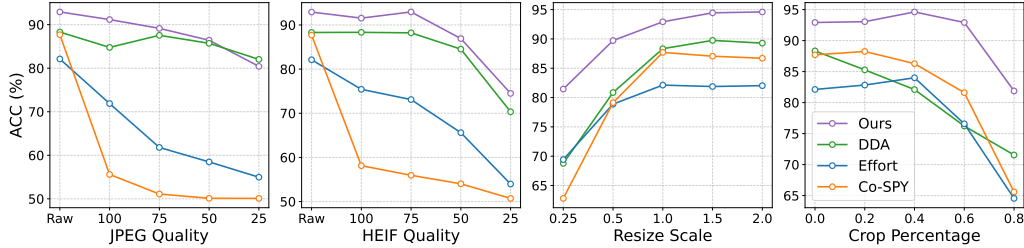


Figure 5: **Robustness Analysis Across Various Perturbations on Established Image Benchmarks.** Degradations include JPEG compression, HEIF compression, scaling, and cropping. Our method consistently outperforms other detectors, demonstrating superior robustness.

Table 7: **Computational Efficiency Comparison.** One RTX 5090 GPU is used in inference.

Method	Params	Resolution	FLOPs	Time / 1K Frames
DDA	306.7M	336 × 336	176.6G	22.3s
B-Free	86.5M	504 × 504	553.7G	77.4s
WaveRep	86.5M	504 × 504	111.2G	24.1s
CO-SPY	513.3M	384 × 384	645.7G	61.8s
Ours	303.1M	256 × 256	82.4G	15.7s

Table 8: **Resolution and Backbone Scaling.** We train DINOv3 models with scaled resolution or backbone size.

Backbone	Resolution	Video	Image	Chameleon	Mean
ViT-L 300M	256 ²	90.4	94.1	91.4	92.0
	384 ²	89.4	96.6	91.6	92.5
	448 ²	90.0	96.2	91.6	92.6
	512 ²	92.5	98.4	91.0	94.0
ViT-H+ 840M	256 ²	90.1	95.9	94.0	<u>93.3</u>

than direct I+V training, suggesting that real video data provides richer and harder-to-simulate degradations. Adding the supervised contrastive loss further improves performance by aligning image and video representations, yielding the best overall result.

4.5 Analysis

Robustness Analysis. As observed in prior work [51, 9], many AIGC image datasets suffer from a *format bias*: real images are typically JPEG-compressed, while generated images are often stored as PNGs. We align formats by applying JPEG compression ($Q = 96$) to all fake PNG images in our four image evaluation sets. As shown in Table 6, this causes a substantial drop for most detectors, whereas our model trained on 140k+SD1.4 remains stable without explicit image-level alignment. The broader perturbation results in Figure 5 further show consistent robustness across JPEG compression, HEIF compression, scaling, and cropping, suggesting that joint video-image training suppresses shortcut learning through natural video regularization.

Computational Efficiency. Table 7 compares the computational cost of representative image and video AIGC detectors under a unified measurement protocol. All methods are evaluated on a single NVIDIA RTX 5090 GPU using FP32 precision, and the batch size is set to 64 or the maximum value allowed by GPU memory for each method. Despite using a large DINOv3 backbone, our model processes frames at 256×256 resolution and requires only 82.4G FLOPs per frame, yielding the fastest throughput at 15.7s per 1K frames. This indicates that the proposed unified detector is not only accurate across image and video benchmarks but also computationally efficient at inference time.

Scaling Spatial Resolution and Backbone. Table 8 evaluates spatial scalability by retraining models at higher input resolutions and with larger backbones. For ViT-L (300M), increasing resolution from 256^2 to 512^2 yields a monotonic improvement in mean accuracy ($92.0 \rightarrow 94.0$), with consistent gains on both image and video benchmarks. Scaling the backbone to ViT-H+ (840M) further improves the 256^2 setting, suggesting that the framework benefits from both higher-resolution inputs and increased model capacity.

5 Conclusion

This paper investigates why state-of-the-art AI-generated image detectors often fail to generalize to video frames. Through an analysis of real-world video acquisition and distribution, we identify synthesis-agnostic domain shifts that overwhelm image-centric forensic cues and model-specific artifacts introduced by modern video generators. Guided by these insights, we propose VINA, a

unified AIGC detection framework and training philosophy that treats realistic video degradations as physically grounded augmentation and enforces consistency across high-quality images and degraded video-style frames. Extensive experiments show that VINA substantially improves cross-domain robustness and achieves strong performance in challenging in-the-wild scenarios.

Limitations. Our detector operates primarily on single frames and does not explicitly model temporal relationships, which may miss artifacts that only emerge through motion inconsistency. In addition, current analysis of model interpretability remains limited. Incorporating temporal reasoning and more faithful attribution analysis could further improve robustness, accuracy, and transparency.

References

- [1] Patrick Esser, Sumith Kulal, Andreas Blattmann, Rahim Entezari, Jonas Müller, Harry Saini, Yam Levi, Dominik Lorenz, Axel Sauer, Frederic Boesel, Dustin Podell, Tim Dockhorn, Zion English, Kyle Lacey, Alex Goodwin, Yannik Marek, and Robin Rombach. Scaling rectified flow transformers for high-resolution image synthesis, 2024. arXiv:2403.03206.
- [2] Tim Brooks, Bill Peebles, Connor Holmes, Will DePue, Yufei Guo, Li Jing, David Schnurr, Joe Taylor, Troy Luhman, Eric Luhman, Clarence Ng, Ricky Wang, and Aditya Ramesh. Video generation models as world simulators, 2024. URL <https://openai.com/index/sora/>.
- [3] Tao Wang, Yushu Zhang, Shuren Qi, Ruoyu Zhao, Zhihua Xia, and Jian Weng. Security and privacy on generative data in aigc: A survey. *ACM Computing Surveys*, 57(4):1–34, 2024.
- [4] Chuangchuan Tan, Yao Zhao, Shikui Wei, Guanghua Gu, Ping Liu, and Yunchao Wei. Rethinking the up-sampling operations in cnn-based generative network for generalizable deepfake detection. In *CVPR*, pages 28130–28139, 2024.
- [5] Ouxiang Li, Jiayin Cai, Yanbin Hao, Xiaolong Jiang, Yao Hu, and Fuli Feng. Improving synthetic image detection towards generalization: An image transformation perspective. In *KDD*, 2025.
- [6] Siyuan Cheng, Lingjuan Lyu, Zhenting Wang, Xiangyu Zhang, and Vikash Sehwal. Co-spy: Combining semantic and pixel features to detect synthetic images by ai. In *CVPR*, 2025.
- [7] Utkarsh Ojha, Yuheng Li, and Yong Jae Lee. Towards universal fake image detectors that generalize across generative models. In *CVPR*, pages 24480–24489, 2023.
- [8] Zhiyuan Yan, Jiangming Wang, Peng Jin, Ke-Yue Zhang, Chengchun Liu, Shen Chen, Taiping Yao, Shouhong Ding, Baoyuan Wu, and Li Yuan. Orthogonal subspace decomposition for generalizable ai-generated image detection. In *ICML*, 2025.
- [9] Ruoxin Chen, Junwei Xi, Zhiyuan Yan, Ke-Yue Zhang, Shuang Wu, Jingyi Xie, Xu Chen, Lei Xu, Isabel Guan, Taiping Yao, and Shouhong Ding. Dual data alignment makes ai-generated image detector easier generalizable. In *NeurIPS*, 2025.
- [10] Fabrizio Guillaro, Giada Zingarini, Ben Usman, Avneesh Sud, Davide Cozzolino, and Luisa Verdoliva. A bias-free training paradigm for more general ai-generated image detection. In *CVPR*, 2025.
- [11] Riccardo Corvi, Davide Cozzolino, Ekta Prashnani, Shalini De Mello, Koki Nagano, and Luisa Verdoliva. Seeing what matters: Generalizable ai-generated video detection with forensic-oriented augmentation. In *NeurIPS*, 2025.
- [12] Davide Cozzolino, Giovanni Poggi, Matthias Nießner, and Luisa Verdoliva. Zero-shot detection of ai-generated images. In *ECCV*, 2024.
- [13] Shilin Yan, Ouxiang Li, Jiayin Cai, Yanbin Hao, Xiaolong Jiang, Yao Hu, and Weidi Xie. A sanity check for ai-generated image detection. In *ICLR*, 2025.
- [14] Chunxiao Li, Xiaoxiao Wang, Meiling Li, Bomang Miao, Peng Sun, Yunjian Zhang, Xiangyang Ji, and Yao Zhu. Bridging the gap between ideal and real-world evaluation: Benchmarking ai-generated image detection in challenging scenarios. In *ICCV*, 2025.

- [15] Haoxing Chen, Yan Hong, Zizheng Huang, Zhuoer Xu, Zhangxuan Gu, Yaohui Li, Jun Lan, Huijia Zhu, Jianfu Zhang, Weiqiang Wang, and Huaxiong Li. Demamba: Ai-generated video detection on million-scale genvideo benchmark, 2024. arXiv:2405.19707.
- [16] Shuhai Zhang, ZiHao Lian, Jiahao Yang, Daiyuan Li, Guoxuan Pang, Feng Liu, Bo Han, Shutao Li, and Mingkui Tan. Physics-driven spatiotemporal modeling for ai-generated video detection. In *NeurIPS*, 2025.
- [17] Weiyun Wang, Min Shi, Qingyun Li, Wenhai Wang, Zhenhang Huang, Linjie Xing, Zhe Chen, Hao Li, Xizhou Zhu, Zhiguo Cao, Yushi Chen, Tong Lu, Jifeng Dai, and Yu Qiao. The all-seeing project: Towards panoptic visual recognition and understanding of the open world, 2023. arXiv:2308.01907.
- [18] Sheng-Yu Wang, Oliver Wang, Richard Zhang, Andrew Owens, and Alexei A. Efros. Cnn-generated images are surprisingly easy to spot... for now. In *CVPR*, pages 8695–8704, 2020.
- [19] Mingjian Zhu, Hanting Chen, Qiangyu Yan, Xudong Huang, Guanyu Lin, Wei Li, Zhijun Tu, Hailin Hu, Jie Hu, and Yunhe Wang. Genimage: A million-scale benchmark for detecting ai-generated image. In *NeurIPS*, 2023.
- [20] Zhengcen Li, Chenyang Jiang, Hang Zhao, Shiyang Zhou, Yunyang Mo, Feng Gao, Fan Yang, Qiben Shan, Shaocong Wu, and Jingyong Su. Preserving forgery artifacts: AI-generated video detection at native scale. In *ICLR*, 2026. URL <https://openreview.net/forum?id=XD431fRCg6>.
- [21] Ian J. Goodfellow, Jean Pouget-Abadie, Mehdi Mirza, Bing Xu, David Warde-Farley, Sherjil Ozair, Aaron Courville, and Yoshua Bengio. Generative adversarial networks. In *NeurIPS*, 2014.
- [22] Diederik P. Kingma and Max Welling. Auto-encoding variational bayes, 2022. arXiv:1312.6114.
- [23] Aaron van den Oord, Oriol Vinyals, and Koray Kavukcuoglu. Neural discrete representation learning, 2018. arXiv:1711.00937.
- [24] Jonathan Ho, Ajay Jain, and Pieter Abbeel. Denoising diffusion probabilistic models. In *NeurIPS*, 2020.
- [25] Robin Rombach, Andreas Blattmann, Dominik Lorenz, Patrick Esser, and Björn Ommer. High-resolution image synthesis with latent diffusion models. In *CVPR*, pages 10684–10695, 2022.
- [26] William Peebles and Saining Xie. Scalable diffusion models with transformers. In *ICCV*, 2023.
- [27] Keyu Tian, Yi Jiang, Zehuan Yuan, Bingyue Peng, and Liwei Wang. Visual autoregressive modeling: Scalable image generation via next-scale prediction. In *NeurIPS*, 2024.
- [28] Chaorui Deng, Deyao Zhu, Kunchang Li, Chenhui Gou, Feng Li, Zeyu Wang, Shu Zhong, Weihao Yu, Xiaonan Nie, Ziang Song, Guang Shi, and Haoqi Fan. Emerging properties in unified multimodal pretraining, 2025. arXiv:2505.14683.
- [29] Uriel Singer, Adam Polyak, Thomas Hayes, Xi Yin, Jie An, Songyang Zhang, Qiyuan Hu, Harry Yang, Oron Ashual, Oran Gafni, Devi Parikh, Sonal Gupta, and Yaniv Taigman. Make-a-video: Text-to-video generation without text-video data, 2022. arXiv:2209.14792.
- [30] Andreas Blattmann, Tim Dockhorn, Sumith Kulal, Daniel Mendelevitch, Maciej Kilian, Dominik Lorenz, Yam Levi, Zion English, Vikram Voleti, Adam Letts, Varun Jampani, and Robin Rombach. Stable video diffusion: Scaling latent video diffusion models to large datasets, 2023. arXiv:2311.15127.
- [31] WanTeam, Ang Wang, Baole Ai, Bin Wen, Chaojie Mao, Chen-Wei Xie, Di Chen, Fei Wu, Haiming Zhao, Jianxiao Yang, Jianyuan Zeng, Jiayu Wang, Jingfeng Zhang, Jingren Zhou, Jinkai Wang, Jixuan Chen, Kai Zhu, Kang Zhao, Keyu Yan, Lianghua Huang, Mengyang Feng, Ningyi Zhang, Pandeng Li, Pingyu Wu, Ruihang Chu, Ruili Feng, Shiwei Zhang, Siyang Sun, Tao Fang, Tianxing Wang, Tianyi Gui, Tingyu Weng, Tong Shen, Wei Lin, Wei Wang, Wei Wang, Wenmeng Zhou, Wenten Wang, Wenting Shen, Wenyuan Yu, Xianzhong Shi, Xiaoming

- Huang, Xin Xu, Yan Kou, Yangyu Lv, Yifei Li, Yijing Liu, Yiming Wang, Yingya Zhang, Yitong Huang, Yong Li, You Wu, Yu Liu, Yulin Pan, Yun Zheng, Yuntao Hong, Yupeng Shi, Yutong Feng, Zeyinzi Jiang, Zhen Han, Zhi-Fan Wu, and Ziyu Liu. Wan: Open and advanced large-scale video generative models, 2025. arXiv:2503.20314.
- [32] Kuaishou. <https://klingai.kuaishou.com>, 2024. URL <https://klingai.kuaishou.com>.
- [33] Yu Gao, Haoyuan Guo, Tuyen Hoang, Weilin Huang, Lu Jiang, Fangyuan Kong, Huixia Li, Jiashi Li, Liang Li, Xiaojie Li, Xunsong Li, Yifu Li, Shanchuan Lin, Zhijie Lin, Jiawei Liu, Shu Liu, Xiaonan Nie, Zhiwu Qing, Yuxi Ren, Li Sun, Zhi Tian, Rui Wang, Sen Wang, Guoqiang Wei, Guohong Wu, Jie Wu, Ruiqi Xia, Fei Xiao, Xuefeng Xiao, Jiangqiao Yan, Ceyuan Yang, Jianchao Yang, Runkai Yang, Tao Yang, Yihang Yang, Zilyu Ye, Xuejiao Zeng, Yan Zeng, Heng Zhang, Yang Zhao, Xiaozheng Zheng, Peihao Zhu, Jiabin Zou, and Feilong Zuo. Seedance 1.0: Exploring the boundaries of video generation models, 2025.
- [34] Zhendong Wang, Jianmin Bao, Wengang Zhou, Weilun Wang, Hezhen Hu, Hong Chen, and Houqiang Li. Dire for diffusion-generated image detection. In *ICCV*, pages 22445–22455, 2023.
- [35] Baoying Chen, Jishen Zeng, Jianquan Yang, and Rui Yang. Drct: Diffusion reconstruction contrastive training towards universal detection of diffusion generated images. In *ICML*, 2024.
- [36] Yanran Zhang, Bingyao Yu, Yu Zheng, Wenzhao Zheng, Yueqi Duan, Lei Chen, Jie Zhou, and Jiwen Lu. $\mathbf{d^3}$: Learning discrete distribution discrepancy-aware quantization error for autoregressive-generated image detection. In *ICCV*, 2025.
- [37] Huan Liu, Zichang Tan, Chuangchuang Tan, Yunchao Wei, Jingdong Wang, and Yao Zhao. Forgery-aware adaptive transformer for generalizable synthetic image detection. In *CVPR*, pages 10770–10780, 2024.
- [38] Christos Koutlis and Symeon Papadopoulos. Leveraging representations from intermediate encoder-blocks for synthetic image detection. In *ECCV*, 2024.
- [39] Chuangchuang Tan, Renshuai Tao, Huan Liu, Guanghua Gu, Baoyuan Wu, Yao Zhao, and Yunchao Wei. C2p-clip: Injecting category common prompt in clip to enhance generalization in deepfake detection. In *AAAI*, volume 39, pages 7184–7192, 2025.
- [40] Tero Karras, Timo Aila, Samuli Laine, and Jaakko Lehtinen. Progressive growing of gans for improved quality, stability, and variation. In *ICLR*, 2018.
- [41] Rohit Kundu, Hao Xiong, Vishal Mohanty, Athula Balachandran, and Amit K. Roy-Chowdhury. Towards a universal synthetic video detector: From face or background manipulations to fully ai-generated content. In *CVPR*, 2025.
- [42] Zhen-Liang Ni, Qiangyu Yan, Tianning Yuan, Mouxiao Huang, Hailin Hu, Xinghao Chen, and Yunhe Wang. Genvidbench: A challenging benchmark for detecting ai-generated video, 2024.
- [43] Chende Zheng, Ruiqi suo, Chenhao Lin, Zhengyu Zhao, Le Yang, Shuai Liu, Minghui Yang, Cong Wang, and Chao Shen. D3: Training-free ai-generated video detection using second-order features. In *ICCV*, 2025.
- [44] Kyoungjun Park, Yifan Yang, Juheon Yi, Shicheng Zheng, Yifei Shen, Dongqi Han, Caihua Shan, Muhammad Muaz, and Lili Qiu. Vidguard-r1: Ai-generated video detection and explanation via reasoning mllms and rl, 2025. arXiv:2510.02282.
- [45] Yifei Li, Wenzhao Zheng, Yanran Zhang, Runze Sun, Yu Zheng, Lei Chen, Jie Zhou, and Jiwen Lu. Skyra: Ai-generated video detection via grounded artifact reasoning, 2025. arXiv:2512.15693.
- [46] Hao Tan, Jun Lan, Senyuan Shi, Zichang Tan, Zijian Yu, Huijia Zhu, Weiqiang Wang, Jun Wan, and Zhen Lei. Videoveritas: Ai-generated video detection via perception pretext reinforcement learning, 2026. arXiv:2602.08828.

- [47] Haiquan Wen, Tianxiao Li, Zhenglin Huang, Yiwei He, and Guangliang Cheng. Busterx++: Towards unified cross-modal ai-generated content detection and explanation with mllm, 2025. arXiv:2507.14632.
- [48] Junyan Ye, Baichuan Zhou, Zilong Huang, Junan Zhang, Tianyi Bai, Hengrui Kang, Jun He, Honglin Lin, Zihao Wang, Tong Wu, Zhizheng Wu, Yiping Chen, Dahua Lin, Conghui He, and Weijia Li. Loki: A comprehensive synthetic data detection benchmark using large multimodal models, 2025. arXiv:2410.09732.
- [49] Wayne Zhang, Changjiang Jiang, Zhonghao Zhang, Chenyang Si, Fengchang Yu, and Wei Peng. Ivy-fake: A unified explainable framework and benchmark for image and video aigc detection, 2025. arXiv:2506.00979.
- [50] Ruoxin Chen, Jiahui Gao, Kaiqing Lin, Keyue Zhang, Yandan Zhao, Isabel Guan, Taiping Yao, and Shouhong Ding. Aligngemini: Generalizable ai-generated image detection through task-model alignment, 2026.
- [51] Anirudh Sundara Rajan, Utkarsh Ojha, Jedidiah Schloesser, and Yong Jae Lee. Aligned datasets improve detection of latent diffusion-generated images. In *ICLR*, 2025.
- [52] Ruiqi Liu, Yi Han, Zhengbo Zhang, Liwei Yao, Zhiyuan Yan, Jialiang Shen, ZhiJin Chen, Boyi Sun, Lubin Weng, Jing Dong, Yan Wang, and Shu Wu. Beyond artifacts: Real-centric envelope modeling for reliable ai-generated image detection, 2025. arXiv:2512.20937.
- [53] Will Kay, Joao Carreira, Karen Simonyan, Brian Zhang, Chloe Hillier, Sudheendra Vijayanarasimhan, Fabio Viola, Tim Green, Trevor Back, Paul Natsev, Mustafa Suleyman, and Andrew Zisserman. The kinetics human action video dataset. *arXiv preprint arXiv:1705.06950*, pages 1–22, 2017.
- [54] Ziqi Huang, Yinan He, Jiashuo Yu, Fan Zhang, Chenyang Si, Yuming Jiang, Yuanhan Zhang, Tianxing Wu, Qingyang Jin, Nattapol Chanpaisit, Yaohui Wang, Xinyuan Chen, Limin Wang, Dahua Lin, Yu Qiao, and Ziwei Liu. Vbench: Comprehensive benchmark suite for video generative models, 2023. arXiv:2311.17982.
- [55] Ricard Durall, Margret Keuper, and Janis Keuper. Watch your up-convolution: Cnn based generative deep neural networks are failing to reproduce spectral distributions. In *CVPR*, 2020.
- [56] Zexi Jia, Chuanwei Huang, Yeshuang Zhu, Hongyan Fei, Xiaoyue Duan, Zhiqiang Yuan, Ying Deng, Jiawei Zhang, Jinchao Zhang, and Jie Zhou. Secret lies in color: Enhancing ai-generated images detection with color distribution analysis. In *CVPR*, pages 13445–13454, 2025.
- [57] Rohit Kundu, Vishal Mohanty, Hao Xiong, Shan Jia, Athula Balachandran, and Amit K. Roy-Chowdhury. Saga: Source attribution of generative ai videos, 2025. arXiv:2511.12834.
- [58] Xingyu Fu, Siyi Liu, Yinuo Xu, Pan Lu, Guangqiuse Hu, Tianbo Yang, Taran Anantasagar, Christopher Shen, Yikai Mao, Yuanzhe Liu, Keyush Shah, Chung Un Lee, Yejin Choi, James Zou, Dan Roth, and Chris Callison-Burch. Learning human-perceived fakeness in ai-generated videos via multimodal llms, 2025. arXiv:2509.22646.
- [59] Prannay Khosla, Piotr Teterwak, Chen Wang, Aaron Sarna, Yonglong Tian, Phillip Isola, Aaron Maschinot, Ce Liu, and Dilip Krishnan. Supervised contrastive learning. In *NeurIPS*, volume 33, pages 18661–18673, 2020.
- [60] Pika Labs. <https://pika.art/>, 2023. URL <https://pika.art/>.
- [61] Davide Cozzolino, Giovanni Poggi, Riccardo Corvi, Matthias Nießner, and Luisa Verdoliva. Raising the bar of ai-generated image detection with clip. In *CVPRW*, 2024.
- [62] Bar Cavia, Eliahu Horwitz, Tal Reiss, and Yedid Hoshen. Real-time deepfake detection in the real-world, 2024. arXiv:2406.09398.
- [63] Ziqiang Li, Jiazhen Yan, Ziwen He, Kai Zeng, Weiwei Jiang, Lizhi Xiong, and Zhangjie Fu. Is artificial intelligence generated image detection a solved problem? In *NeurIPS*, 2025.

- [64] Ruiqi Liu, Manni Cui, Ziheng Qin, Zhiyuan Yan, Ruoxin Chen, Yi Han, Zhiheng Li, Junkai Chen, ZhiJin Chen, Kaiqing Lin, Jialiang Shen, Lubin Weng, Jing Dong, Yan Wang, and Shu Wu. Mirror: Manifold ideal reference reconstructor for generalizable ai-generated image detection, 2026. arXiv:2602.02222.
- [65] Alec Radford, Jong Wook Kim, Chris Hallacy, Aditya Ramesh, Gabriel Goh, Sandhini Agarwal, Girish Sastry, Amanda Askell, Pamela Mishkin, Jack Clark, Gretchen Krueger, and Ilya Sutskever. Learning transferable visual models from natural language supervision, 2021. arXiv:2103.00020.
- [66] Maxime Oquab, Timothée Darcet, Théo Moutakanni, Huy V. Vo, Marc Szafraniec, Vasil Khalidov, Pierre Fernandez, Daniel Haziza, Francisco Massa, Alaaeldin El-Nouby, Mido Assran, Nicolas Ballas, Wojciech Galuba, Russell Howes, Po-Yao Huang, Shang-Wen Li, Ishan Misra, Michael Rabbat, Vasu Sharma, Gabriel Synnaeve, Hu Xu, Herve Jegou, Julien Mairal, Patrick Labatut, Armand Joulin, and Piotr Bojanowski. Dinov2: Learning robust visual features without supervision. *Transactions on Machine Learning Research*, 2023. ISSN 2835-8856.
- [67] Oriane Siméoni, Huy V. Vo, Maximilian Seitzer, Federico Baldassarre, Maxime Oquab, Cijo Jose, Vasil Khalidov, Marc Szafraniec, Seungeun Yi, Michaël Ramamonjisoa, Francisco Massa, Daniel Haziza, Luca Wehrstedt, Jianyuan Wang, Timothée Darcet, Théo Moutakanni, Leonel Sentana, Claire Roberts, Andrea Vedaldi, Jamie Tolan, John Brandt, Camille Couprie, Julien Mairal, Hervé Jégou, Patrick Labatut, and Piotr Bojanowski. Dinov3, 2025. arXiv:2508.10104.

Appendix

The appendix is organized as follows.

- **Section A: Dataset Analysis.** Additional frequency-domain analysis of image and video datasets.
- **Section B: Implementation Details.** Baseline checkpoints, preprocessing, and inference settings.
- **Section C: Detailed Benchmark Results.** Extended results on image- and video-based AIGC detection benchmarks.
- **Section D: More Ablation Studies.** Additional analyses of data sources, tuning, image transforms, and CM-SupCon loss weights.
- **Section E: Scaling Potentials.** Temporal scaling results.
- **Section F: Discussion.** Broader impacts and deployment risks.

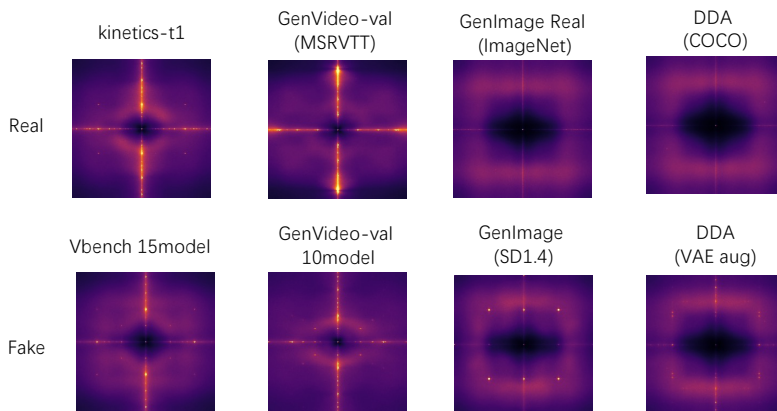


Figure 6: **2D power spectra of reconstructed noise.** Spectra are averaged over 1,000 samples. Videos exhibit a distinct axial cross pattern, in contrast to the broader spectral spread of images. Generated images show periodic grid artifacts, while generated videos display a different configuration of spectral anomalies. This highlights a fundamental divergence in the frequency-space fingerprints of video and image generative models.

A Dataset Analysis

This section includes the spectral visualizations in figs. 6 and 7.

The spectral analysis in figs. 6 and 7 reveals a fundamental divergence between the noise distributions of image and video modalities. We follow the implementation in [11] and randomly select 1k samples from each subset. In real-world data, video exhibits distinct frequency characteristics, shaped by temporal factors like motion blur and artifacts from video compression codecs (e.g., H.264/H.265). Beyond natural content, we observe that generative models imprint distinct architectural traces in the Fourier domain. Critically, a significant gap exists between the spectral patterns of video generation models (e.g., Sora, Gen-2) and image-based Diffusion Transformers (e.g., FLUX, SD3). While image generators often produce periodic, grid-like artifacts, video models induce more complex spatio-temporal frequency distortions. This discrepancy implies that forensic models trained solely on image-based synthetic data face an inherent generalization bottleneck when applied to video, due to this pronounced distribution shift. Consequently, we posit that a joint training paradigm is essential for building a robust and universal detection framework.

B Implementation Details

This section documents the evaluation settings used for the main and appendix comparisons in tables 1, 2 and 10.

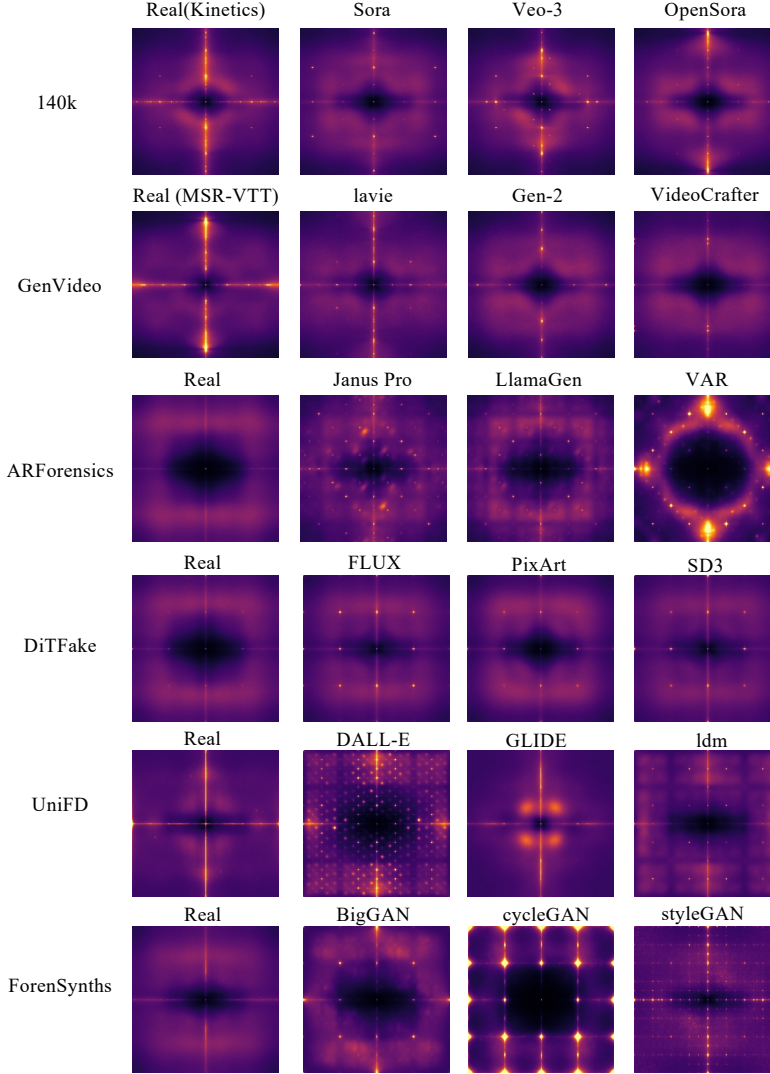


Figure 7: **Average Fourier power spectra across different generative models and datasets.** The visualizations compare the frequency-domain characteristics of real data (leftmost column) against various image and video generation frameworks. Note the unique structural artifacts (e.g., grid patterns) present in the generated samples across different model families.

1. **WaveRep** [11] trains DINO classifiers toward intrinsic low-level artifacts through wavelet-based data augmentation and discriminative feature analysis to enhance generalizability for AIGV detection. We use their released weights and adopt the same 504p crop preprocessing method as their original implementation.
2. **Effort** [8] is a parameter-efficient method that leverages SVD to construct orthogonal subspaces. This design prevents catastrophic forgetting of pre-trained semantic knowledge while efficiently learning forgery patterns. Our implementation uses their released weights trained on SD1.4 with identical preprocessing.
3. **NPR** [4] distinguishes synthetic images by analyzing low-level neighboring pixel relationships, which are characteristic of upsampling patterns in AI-generated content. It implements this approach by training a ResNet-50 model for identification. We use their official checkpoint for evaluation.
4. **RINE** [38] improves AI-generated image detection by mapping intermediate CLIP features to a forgery-aware vector space. We utilize the author-released weights trained on the

Table 9: **Overview of the evaluation benchmarks.** Our evaluation covers 14 benchmarks (4 video benchmarks, 5 image benchmarks, and 5 in-the-wild benchmarks), spanning a diverse range of generator architectures to ensure broad and comprehensive assessment.

Dataset	Type	Real/Fake	Model Types
Magic Videos [20]	Video	0.5k/1.5k	DiT, Commercial
GenVideo [15]	Video	10k/9.5k	SVD, DiT
Genbuster++ [47]	Video	1k/1k	Commercial
DeepTraceReward [58]	Video	3.3k/3.3k	Commercial
ForenSynths [18]	Image	45k/45k	GAN, Deepfake
UniFD [7]	Image	8k/8k	LDM
DiTFake [5]	Image	15k/15k	DiT
ARforensics [36]	Image	39k/39k	Auto-Regressive
GenImage [19]	Image	48K/48K	SD, GAN
Chameleon [13]	in-the-wild	14.9k/11.2k	in-the-wild
SynthWildx [61]	in-the-wild	500/1.5K	X
WildRF [62]	in-the-wild	500/500	unknown
AIGIBench [63]	in-the-wild	9k/9k	SocialRF, CommunityAI
RR-Dataset [14]	in-the-wild	25k/25k	SD3.5, FLUX.1

ProGAN 4class dataset and adopt the same resize preprocessing method as the original implementation.

- B-Free** [10] employs a self-conditioned diffusion reconstruction paradigm to enforce semantic alignment between real and synthetic images, thereby isolating differences to generation artifacts. The method incorporates content augmentation via inpainting and fine-tunes a DINOv2+reg ViT using large crops to preserve forensic signals. We utilize their provided checkpoint, applying the same 504p five-crop preprocessing.
- CO-SPY** [6] enhances semantic and artifact features for robust synthetic image detection. Following the official code, we evaluate the two author-released implementations trained on SD1.4 and ProGAN.
- DDA** [9] aligns synthetic and real images in both pixel and frequency domains to mitigate spurious correlations and improve detector generalization. For evaluation, we utilize the author-released weights and identical settings, with the sole exception that we forgo applying the same JPEG Q=96 compression on the test sets to ensure a fair comparison with other methods. Our results show that applying or forgoing this specific JPEG compression has a negligible impact on the performance of both the DDA method and our approach.

C Detailed Benchmark Results

This section includes the benchmark overview and detailed results in tables 9 to 17.

Performance Comparison in AP. Table 10 complements the ACC comparison in table 1 by evaluating ranking quality across the same video and image benchmarks. Video-specific detectors such as DeMamba and Qwen2.5-ViT achieve higher AP on video benchmarks than on image datasets, while image-based detectors show the opposite tendency and often lose discriminative ranking on videos. In contrast, joint video-image training produces consistently high AP across both modalities. The strongest VINA model achieves 97.70% video AP, 99.08% image AP, and 98.39% overall AP, indicating that the proposed framework improves not only threshold-dependent accuracy but also cross-domain ranking robustness.

Performance on GenImage. Table 11 presents a comprehensive benchmark comparison on the GenImage dataset [19], evaluating VINA against several state-of-the-art detectors across eight diverse generative models. We evaluate all methods using their released checkpoints and the corresponding test transformations. VINA achieves strong performance without JPEG alignment (94.74% AVG) and further improves to 95.53% AVG with the JPEG setting, outperforming the strongest image-only

Table 10: **Comparison results on 4 video-based and 4 image-based AIGC detection benchmarks in AP(%)**. Except for DeMamba, for which no public checkpoint is available and which we retrain on GenVideo-100k, all results are obtained by us using the authors’ released pretrained weights and the corresponding inference-time transform settings.

Method	Type	Video					Image					ALL AVG
		AVG	Magic	GenVideo	GenBuster++	DeepTrace Reward	AVG	ForenSynths (GAN)	UniFD (LDM)	DiTFake	ARForensics	
DeMamba [15] (100k)	Video	84.21	73.78	96.66	68.49	97.90	65.40	56.50	57.00	84.96	63.14	74.81
Qwen2.5-ViT [20]	Video	95.80	96.94	99.52	87.86	98.89	71.17	52.64	62.38	95.16	74.48	83.48
WaveRep [11]	Video	90.09	88.99	98.18	73.92	99.26	96.01	98.87	93.83	98.91	92.42	93.05
NPR [4]	Image	67.83	70.19	65.26	68.89	66.96	84.34	78.85	96.22	83.37	78.93	76.08
FatFormer [37]	Image	53.98	40.19	63.48	52.03	60.23	88.46	97.88	98.56	70.03	87.37	71.22
RINE [38]	Image	61.73	35.48	91.06	71.99	48.38	96.77	98.80	98.96	92.45	96.85	79.25
Effort [8]	Image	80.67	74.05	96.86	67.78	83.99	89.07	78.30	96.79	91.79	89.41	84.87
Co-Spy [6]	Image	83.41	71.16	87.16	82.77	92.56	86.01	70.69	84.21	99.30	89.83	84.71
Co-Spy (ProGAN)	Image	62.31	51.41	58.08	75.43	64.30	93.97	87.79	98.68	96.68	92.72	78.14
DDA [9]	Image	87.87	85.47	92.75	80.57	92.69	94.79	89.06	93.59	99.89	96.61	91.33
B-Free [10]	Image	86.45	80.37	98.06	77.50	89.88	97.00	94.04	96.23	99.43	98.28	91.72
VINA (Pika+ProGAN)	V+I	90.78	79.25	96.64	88.91	98.33	98.55	97.69	98.74	99.54	98.22	94.67
VINA (GenVideo+SD1.4)	V+I	90.58	79.60	98.88	85.21	98.63	98.49	97.35	98.36	99.93	98.32	94.54
VINA (140k+DDA)	V+I	97.70	95.10	99.26	96.53	99.89	99.08	97.77	99.01	99.95	99.60	98.39

baseline (DDA, 88.98%) by 6.55%. Notably, the JPEG variant improves robustness on GLIDE, VQDM, and BigGAN while maintaining near-perfect detection accuracy on the Stable Diffusion and Wukong subsets. The fact that JPEG compression further improves VINA, rather than degrading it, suggests that joint video-image training suppresses shortcut learning from format artifacts and learns more robust generative cues.

Table 11: **Benchmarking results on GenImage [19] in terms of ACC(%)**.

Method	Type	Midjourney	SDv1.4	SDv1.5	ADM	GLIDE	Wukong	VQDM	BigGAN	AVG
WaveRep [11]	V	80.57	82.75	82.76	75.47	78.33	82.17	78.20	82.63	80.36
NPR [4]	I	77.73	78.23	78.83	74.22	78.87	72.40	77.84	81.28	77.43
FatFormer [37]	I	56.08	67.83	68.06	78.44	88.03	73.06	86.88	96.79	76.90
RINE [38]	I	57.12	83.94	83.36	74.58	80.71	84.94	89.76	94.83	81.16
Effort [8]	I	76.17	87.77	87.61	70.88	80.82	86.81	82.62	75.43	81.01
CO-SPY [6]	I	69.87	93.03	92.9	58.15	81.06	91.03	71.96	64.22	77.78
CO-SPY (ProGAN)	I	86.98	85.40	85.58	78.79	91.26	80.28	84.86	93.57	85.84
DDA [9]	I	96.00	98.57	98.53	88.03	86.13	98.61	71.83	74.11	88.98
VINA (140k+DDA)	V+I	96.11	99.89	99.85	76.23	94.65	99.83	94.98	96.38	94.74
VINA (140k+DDA, JPEG)	V+I	93.83	99.86	99.83	76.79	98.47	99.86	98.08	97.52	95.53

Detailed Performance on ForenSynths. Table 12 reports the cross-method generalization performance on ForenSynths [18] across multiple GAN families, Deepfakes, and low-level/perceptual-loss manipulations using accuracy (ACC) and average precision (AP). RINE achieves the best average ACC (91.79%), while WaveRep achieves the best average AP (98.87%). Several prior methods exhibit high AP but significantly lower ACC on specific subsets, indicating inconsistent decision calibration under distribution shift. VINA achieves the second-best average ACC (86.99%) and competitive AP (97.78%), with strong performance on most GAN categories but a clear degradation on Deepfakes.

Detailed Performance on UniFD(LDM). Table 13 presents cross-method evaluations on the UniversalFakeDetect (LDM) dataset, comparing VINA against several state-of-the-art detection frameworks. VINA achieves the best average accuracy of 94.84%, slightly surpassing the strongest baseline CO-SPY (ProGAN). It also obtains the best average AP of 99.01%, demonstrating strong ranking robustness across LDM, GLIDE, and DALL-E subsets.

Detailed Performance on DiTFake. Table 14 reports cross-method results on DiTFake [5] across FLUX, PixArt, and SD3. DDA achieves the best mACC (98.59), while VINA attains the best mAP (99.95) and reaches 100.0 ACC/AP on PixArt. Overall, VINA remains consistently high across generators with near-saturated AP.

Detailed Performance on ARForensics. Table 15 evaluates cross-method generalization on ARForensics [36], which consists of previously unseen auto-regressive generator architectures (e.g.,

Table 12: **Benchmarking Results of Cross-method Evaluations in terms of ACC(%) and AP(%) Performance on the ForenSynth [18] Dataset.** All evaluations used the authors’ provided checkpoints and preprocessing pipelines.

Methods	Type	GAN						Deep fakes	Low level		Perceptual loss		AVG
		Pro-GAN	Cycle-GAN	Big-GAN	Style-GAN	Gau-GAN	Star-GAN		SITD	SAN	CRN	IMLE	
WaveRep [11]	ACC	92.99	72.67	73.28	90.80	70.16	94.50	87.64	84.44	80.59	58.54	58.54	78.56
	AP	99.85	98.53	96.41	97.56	99.61	99.87	96.65	99.68	99.41	100.0	100.0	98.87
RINE [38]	ACC	100.00	99.28	99.60	92.09	99.77	99.55	80.63	90.56	68.26	89.24	90.67	91.79
	AP	100.00	99.99	99.94	99.79	100.00	100.00	97.90	97.22	94.93	97.26	99.74	<u>98.80</u>
Effort (SD1.4) [8]	ACC	83.62	92.51	86.83	80.42	82.14	98.95	69.40	58.33	52.74	51.91	51.74	73.51
	AP	92.59	94.46	86.12	86.72	80.65	99.89	75.22	62.16	52.91	68.32	62.27	78.30
NPR [4]	ACC	99.79	91.29	82.12	96.75	78.31	85.99	79.44	58.89	65.30	50.00	50.00	76.17
	AP	99.98	93.53	83.33	99.18	80.70	99.97	82.35	61.29	66.99	50.01	50.01	78.85
DDA [9]	ACC	92.30	63.93	83.62	86.79	89.94	66.28	71.21	72.22	94.29	87.35	90.21	81.65
	AP	99.04	81.23	94.31	94.71	96.91	69.06	82.61	70.77	98.80	93.94	98.25	89.06
CO-SPY (ProGAN)	ACC	100.00	99.28	94.60	97.20	95.16	99.60	77.80	70.00	77.40	50.68	50.68	82.95
	AP	100.00	99.38	98.19	99.98	98.10	100.00	95.15	65.33	83.24	63.18	63.18	87.79
CO-SPY [6]	ACC	74.25	57.87	71.25	61.50	69.26	62.06	65.42	51.94	71.92	54.07	44.84	62.22
	AP	77.64	55.66	83.66	66.65	82.95	94.35	80.00	58.32	79.25	57.26	41.80	70.69
VINA (140k+DDA)	ACC	95.21	93.15	95.05	93.42	96.06	98.2	63.16	85.28	83.79	76.83	76.79	<u>86.99</u>
	AP	99.35	99.52	99.81	97.84	99.96	99.97	90.77	95.43	95.16	99.6	98.12	97.78

Table 13: **Benchmarking Results on UniversalFakeDetect (LDM) [7]: Accuracy and Average Precision.** All evaluations used the authors’ provided checkpoints and preprocessing pipelines.

Method	Type	guided	ldm_200	ldm_200_cfg	ldm_100	glide_100_27	glide_50_27	glide_100_10	dalle	AVG
WaveRep [11]	ACC	79.40	78.80	81.45	76.70	79.45	80.85	82.85	84.10	80.45
	AP	88.93	92.66	95.57	90.66	93.17	94.32	96.81	98.53	93.83
FatFormer [37]	ACC	76.05	96.70	94.85	98.60	94.30	94.60	94.15	98.70	93.49
	AP	91.92	99.53	99.22	99.89	99.27	99.50	99.33	99.84	98.56
RINE [38]	ACC	76.15	93.27	88.25	98.65	88.95	92.60	90.70	95.10	90.46
	AP	96.56	99.31	98.71	99.91	99.08	99.45	99.16	99.48	<u>98.96</u>
Effort (SD1.4) [8]	ACC	78.05	93.80	91.70	96.45	93.05	91.60	92.05	96.65	91.67
	AP	84.34	98.57	97.83	99.35	98.53	98.02	98.30	99.41	96.79
NPR [4]	ACC	74.40	96.67	96.60	96.15	96.20	96.80	96.95	88.70	92.81
	AP	79.51	98.91	98.85	98.87	98.91	98.92	98.99	96.78	96.22
DDA [9]	ACC	90.45	84.12	84.20	83.95	75.25	74.70	79.85	72.05	80.57
	AP	98.17	99.26	99.36	99.11	88.22	87.42	92.88	84.28	93.59
CO-SPY (ProGAN)	ACC	79.45	95.88	94.55	97.55	97.00	97.85	97.85	94.85	<u>94.37</u>
	AP	91.18	99.68	99.54	99.80	99.83	99.89	99.87	99.61	98.68
CO-SPY [6]	ACC	62.40	83.53	84.85	82.00	72.85	68.20	75.40	81.30	79.01
	AP	85.93	89.29	91.00	86.83	77.91	74.33	81.40	87.13	84.23
VINA (140k+DDA)	ACC	75.80	99.30	99.30	99.30	94.45	96.10	96.55	97.95	94.84
	AP	93.98	99.99	99.99	99.99	99.30	99.45	99.59	99.81	99.01

Infinity, Janus Pro, VAR). VINA achieves the best overall performance, reaching 96.74 AVG ACC and 99.59 AVG AP. Compared to prior detectors, which exhibit larger accuracy drops on these out-of-distribution AR generators, the results indicate stronger robustness of unified training to novel generator architectures.

Detailed Performance on Magic Videos. The Magic Videos dataset primarily comprises high-resolution videos generated by state-of-the-art commercial models, presenting a significant challenge for current detection frameworks. As shown in table 16, existing AI image and video detection methods struggle to maintain robust performance on this benchmark, with most baselines failing to achieve satisfactory results. In contrast, VINA demonstrates superior generalization, achieving the best average accuracy (77.08%) and average precision (95.10%).

Table 14: **Benchmarking Results of Cross-method Evaluations in terms of ACC(%) and AP(%) Performance on the DiTFake [5].** † indicates that the results are obtained by us using the official pre-trained checkpoint and input data transformation.

Method	FLUX	PixArt	SD3	mACC	FLUX	PixArt	SD3	mAP
WaveRep [11]	85.26	86.92	87.01	86.40	97.53	99.70	99.20	98.81
FatFormer [37]	54.49	67.16	58.34	60.00	61.85	79.11	69.12	70.03
RINE [38]	56.27	59.59	55.12	56.99	92.29	93.43	91.62	92.45
Effort [8]	82.00	82.20	82.49	82.23	88.95	94.73	91.70	91.79
Co-SPY [6]	91.13	95.86	93.24	93.41	99.06	99.60	99.23	99.30
DDA [9]	97.15	99.47	99.14	98.59	99.71	99.99	99.96	<u>99.89</u>
VINA (140k+DDA)	97.11	100.0	96.84	<u>97.98</u>	99.95	100.0	99.90	99.95

Table 15: **Benchmarking Results of Cross-method Evaluations in terms of ACC(%) and AP(%) Performance on the ARForensics [36] Dataset.** † indicates that the results are directly from their papers.

Method	Metric	Infinity	Janus Pro	Llama Gen	MAR	MAG VIT2	RAR	VAR	AVG
D ³ QE† [36]	ACC	62.88	97.53	82.11	-	70.08	91.69	85.33	82.11
	AP	79.39	97.53	99.43	-	95.98	97.77	95.30	92.07
FatFormer [37]	ACC	53.67	84.88	69.73	87.33	73.00	98.12	87.01	79.11
	AP	57.84	93.36	83.68	95.20	86.07	99.81	95.66	87.37
RINE [38]	ACC	72.91	84.30	71.74	83.42	67.77	99.03	73.72	78.98
	AP	95.57	98.22	96.53	98.09	93.26	99.96	96.34	<u>96.85</u>
Effort (SD1.4) [8]	ACC	86.84	87.69	79.36	77.42	73.30	85.92	81.55	81.73
	AP	94.06	98.46	88.18	83.96	80.23	90.41	90.58	89.41
CO-SPY (SD1.4) [6]	ACC	93.09	79.68	60.10	65.88	59.21	64.98	63.12	69.44
	AP	99.16	95.89	83.93	89.18	83.09	88.93	88.61	89.83
CO-SPY (ProGAN) [6]	ACC	93.67	79.47	76.08	84.23	77.68	94.16	94.11	85.63
	AP	98.21	87.90	87.38	90.84	87.42	98.60	98.65	92.71
DDA [9]	ACC	98.04	98.47	93.38	93.83	67.31	85.83	75.78	<u>87.52</u>
	AP	99.84	99.90	98.66	99.03	88.40	97.51	92.96	96.61
VINA (140k+DDA)	ACC	99.84	99.90	98.07	99.01	84.08	98.17	98.11	96.74
	AP	100.0	100.0	99.77	99.95	97.56	99.96	99.92	99.59

Detailed Performance on GenVideo-Val. As observed in table 17, most image-based detectors (e.g., NPR, FatFormer) fail significantly on the GenVideo-Val benchmark [15], whereas DDA maintains high recall but suffers from low F1 and AP scores. This discrepancy suggests that image detectors are still capable of perceiving forgery artifacts, yet their decision thresholds are severely disrupted by the inherent domain gap and the lower noise levels characteristic of video data. By introducing video samples as physically augmented regularization, VINA effectively recalibrates the discriminative boundary, achieving the best comprehensive performance with 93.20% average recall, 81.52% average F1, and 92.83% average AP.

D More Ablation Studies

This section includes additional ablation results in tables 18 to 20 and fig. 8.

Ablation Study on Data Sources. Table 18 uses a DINOv3-L backbone without SupCon loss to isolate the effect of training data composition. Performance improves substantially when video

Table 16: **Benchmarking Results in terms of ACC and AP Performance on Magic Videos Testset [20].**

Model	Metric	Wan 2.1	Wan-1.3B	Hailuo	Seaweed	Seedance	StepVideo	AVG
WaveRep [11]	ACC	56.98	53.77	58.84	58.84	56.74	58.60	57.30
	AP	82.13	86.22	94.93	99.16	80.38	91.10	<u>88.99</u>
FatFormer [37]	ACC	50.00	46.75	50.00	50.00	50.00	50.00	49.46
	AP	38.95	34.66	41.22	39.97	36.89	48.99	40.11
RINE [38]	ACC	40.47	41.27	40.70	48.14	39.53	45.81	42.65
	AP	32.62	31.12	32.79	47.24	31.35	42.01	36.19
NPR [4]	ACC	50.23	47.60	50.23	50.93	50.23	50.00	49.87
	AP	64.86	40.01	56.91	87.61	75.41	87.88	68.78
Effort [8]	ACC	83.95	35.79	69.30	81.63	77.21	56.51	67.40
	AP	90.87	35.89	78.97	87.96	87.47	63.14	74.05
Co-SPY [6]	ACC	68.84	59.93	63.26	64.65	57.91	77.67	65.38
	AP	75.40	62.44	70.39	71.99	59.55	90.42	71.70
DDA [9]	ACC	66.28	79.28	77.44	85.81	62.33	69.30	<u>73.41</u>
	AP	76.78	94.22	90.14	97.90	71.62	79.73	85.07
VINA (140k+DDA)	ACC	75.35	89.90	74.19	73.02	74.42	75.58	77.08
	AP	95.44	98.07	94.47	90.51	95.00	97.09	95.10

data is supplemented with real images, or when image data is supplemented with synthetic videos. The best mean accuracy is achieved when the complete dataset containing both modalities is used, highlighting the positive contribution of diverse video and image sources.

Ablation Study on Tuning Method. Table 19 compares tuning strategies on the same 140k+DDA training set. Linear probing underperforms substantially (Mean 76.9), especially on Chameleon, while LoRA yields large gains across all evaluation groups and improves the mean accuracy to 89.9. End-to-end fine-tuning achieves the best overall mean accuracy (92.0), with the strongest video and image performance.

Ablation Study on Image Transforms. Table 20 studies the effect of input transformations using a DINOv3-L detector trained on the 140k+DDA dataset without SupCon loss. Standard cropping introduces a clear trade-off across test settings: for example, center crop improves Image accuracy but substantially degrades Chameleon accuracy, indicating reduced robustness to variations in resolution and framing. The shorter-resize plus random-crop strategy achieves the best mean score (91.41) and the highest Video accuracy (90.29), demonstrating more consistent performance across diverse high- and variable-resolution inputs.

Ablation Study on SupCon Loss Weight. Figure 8 evaluates the sensitivity to the supervised contrastive loss weight λ using the same DINOv3-L model trained on the 140k+DDA dataset. Here, AVG ACC denotes the average accuracy over all 14 benchmarks used in our evaluation. We compare our CM-SupCon loss with a vanilla SupCon variant that treats all samples with the same real/fake label as positives, regardless of modality. CM-SupCon obtains a clear gain over the no-SupCon baseline and reaches the best result at $\lambda = 0.05$ (91.51), while vanilla SupCon provides only marginal improvement and peaks at $\lambda = 0.1$ (90.58). Larger weights reduce performance for both variants, especially when $\lambda = 0.5$, indicating that excessive contrastive regularization can over-constrain the representation and interfere with binary classification.

E Scaling Potentials

This section includes temporal scaling results in table 21.

We investigate whether the same trained model can leverage longer video context by simply increasing the number of sampled frames at inference, without modifying training. Unless otherwise specified, these experiments use DINOv3-L models trained without SupCon loss.

Table 17: **Benchmarking Evaluation in terms of Recall, F1 score (F1), and average precision (AP) on GenVideo-Val [15].** † indicates that the results are directly from their papers.

Model	Metric	Sora	Morph Studio	Gen2	HotShot	Lavie	Show-1	Moon Valley	Crafter	Model Scope	Wild Scrape	Avg.
UNITE [41]	Recall	92.11	100.0	94.62	96.93	98.12	99.86	98.69	100.0	96.29	89.89	89.60
	F1	-	-	-	-	-	-	-	-	-	-	-
	AP	88.57	100.0	100.0	90.16	89.91	98.34	99.52	100.0	98.96	92.56	92.76
WaveRep [11]	Recall	87.50	99.57	100.00	80.00	95.21	97.71	100.00	99.93	97.57	81.93	87.50
	F1	7.78	54.62	70.50	46.38	68.57	53.88	52.01	70.73	53.82	53.39	53.17
	AP	41.93	99.20	99.93	67.55	92.95	93.85	99.70	99.71	94.78	77.39	86.70
NPR [4]	Recall	3.57	7.00	2.83	1.29	2.00	0.00	0.32	3.00	16.71	3.35	4.01
	F1	5.33	12.79	5.43	2.48	3.88	0.00	0.62	5.77	28.06	6.37	7.07
	AP	2.06	39.20	27.84	7.06	16.73	7.31	8.74	45.43	45.78	23.09	22.32
FatFormer [37]	Recall	1.79	2.57	1.23	0.14	2.36	4.14	0.00	4.01	37.00	11.02	6.43
	F1	3.08	4.96	2.42	0.28	4.58	7.87	0.00	7.66	53.57	19.69	10.41
	AP	0.79	22.45	15.46	8.33	24.48	18.87	5.80	31.26	64.30	40.51	23.23
RINE [38]	Recall	28.57	5.86	1.01	2.29	5.14	3.14	2.40	5.51	23.43	7.78	8.51
	F1	42.11	11.01	2.00	4.44	9.76	6.06	4.65	10.41	37.79	14.37	14.26
	AP	64.76	65.22	63.58	36.26	62.23	48.29	46.74	77.39	86.18	63.24	61.39
Effort [8]	Recall	33.93	68.29	56.16	29.86	51.79	40.14	75.24	63.88	77.86	49.78	54.69
	F1	25.17	76.24	69.48	42.44	65.88	53.17	80.31	75.45	82.51	63.01	63.37
	AP	30.81	87.26	89.00	59.99	84.29	71.67	89.36	90.56	91.56	77.43	77.19
Co-SPY [6]	Recall	48.21	96.00	93.62	18.71	53.71	71.29	97.92	90.77	91.71	72.94	73.49
	F1	3.00	43.52	58.89	10.29	38.88	34.24	41.49	57.91	41.99	40.68	37.09
	AP	1.97	76.57	79.94	7.96	37.70	37.98	78.24	76.67	68.19	51.72	51.69
DDA [9]	Recall	51.79	97.29	98.77	98.86	97.64	98.86	97.92	97.85	90.43	82.03	91.14
	F1	0.89	17.37	29.62	17.63	29.63	17.63	15.92	29.66	16.25	18.62	19.32
	AP	0.54	65.57	91.55	80.03	84.67	85.75	81.24	84.50	58.62	52.69	68.52
VINA (140k+DDA)	Recall	75.00	99.86	100.0	94.29	97.71	96.29	100.0	99.79	98.71	70.35	93.20
	F1	29.79	88.31	93.75	85.49	92.68	86.52	87.19	93.72	87.75	73.95	81.52
	AP	56.82	99.74	99.96	95.90	99.03	97.53	99.97	99.87	99.08	80.42	92.83

Table 18: **Ablation study on training data source.** Video Data All = 140k, Image Data All = GenImage SD1.4 Subset. Experiments use a DINOv3-L backbone without SupCon loss.

Video Data (140k)	Image Data (GenImage)	Video AVG	Image AVG	Chame leon	Mean ACC
ALL	-	88.74	79.77	49.45	72.65
ALL	Real	85.51	78.35	89.47	84.44
ALL	Fake	86.08	74.28	47.69	69.35
-	ALL	59.60	75.08	59.49	64.72
Real	ALL	55.64	79.69	60.58	65.30
Fake	ALL	64.63	83.41	88.03	78.69
ALL	ALL	89.79	87.31	91.48	89.53

Scaling Temporal Frames. Table 21 probes temporal scalability by increasing the number of sampled frames per video only at test time (from $T = 1$ to $T = 8$), without changing training. Performance remains stable and slightly improves when using more frames, with mean ACC peaking at 90.59 for $T = 2$. In future work, we will explore increasing the number of sampled frames during training and explicitly modeling temporal dynamics to further benefit from longer temporal context.

Table 19: **Ablation Study on Tuning Methods.** All methods are DINOv3-L backbones trained on 140k+DDA dataset. For LoRA, lr=1e-5 and for LP, lr=1e-4.

Method	Video ACC	Image ACC	Chameleon	Mean
LP	82.2	83.2	65.4	76.9
LoRA (r=16)	89.7	89.0	91.0	<u>89.9</u>
Full (Ours)	90.4	94.1	91.4	92.0

Table 20: **Ablation Study on Training Image Transform Methods.** All methods use a DINOv3-L backbone trained on the 140k+DDA dataset without SupCon loss, with target resolution 256×256 .

Method	Video ACC	Image ACC	Chameleon	Mean
resize	88.13	92.59	90.36	90.36
center crop	87.27	93.93	79.97	87.06
random crop	86.38	96.31	82.73	88.47
random resized crop	88.45	95.57	88.10	<u>90.71</u>
shorter resize + random crop (Ours)	90.29	92.96	90.98	91.41

Table 21: **Test-time temporal scaling.** We vary the number of uniformly sampled frames per video at inference (T) while keeping the DINOv3-L model trained without SupCon loss fixed; logits from multiple frames are averaged.

Sampled Frame	Magic	GenVideo	GenBuster++	DeepTraceReward	Mean
T=1	80.18	96.78	86.35	97.85	90.29
T=2	79.89	97.01	87.3	98.16	90.59
T=4	79.14	97.23	87.45	98.33	<u>90.54</u>
T=8	77.67	97.35	88.05	98.46	<u>90.38</u>

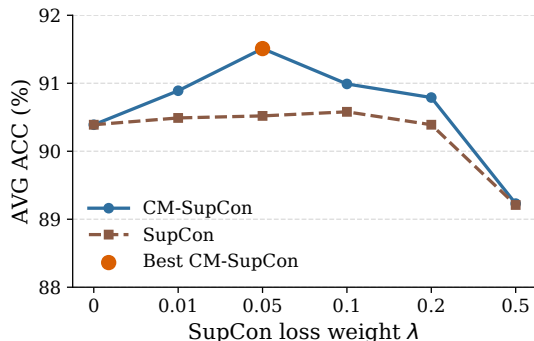


Figure 8: **Ablation Study on SupCon Loss Weight.** We vary the supervised contrastive loss weight λ and report AVG ACC, computed as the average accuracy over all 14 benchmarks. CM-SupCon defines positives across modalities with the same real/fake label, whereas vanilla SupCon uses all same-label samples as positives. CM-SupCon achieves the best result at $\lambda = 0.05$.

F Discussion

Broader Impacts. This work focuses on detecting AI-generated images and videos, rather than introducing or improving AIGC generation techniques. By improving cross-modal detection robustness, VINA can help reduce misunderstanding and misinformation caused by synthetic media, supporting content verification, platform moderation, and forensic analysis.

At the same time, detection research can have dual-use risks. Insights into detector behavior may be used to improve generation pipelines or post-processing strategies that evade current detectors. In practical deployment, another risk is over-confidence: no detector is perfect, and false positives or false negatives may lead to unfair moderation decisions, misplaced trust, or incorrect attribution. We therefore recommend using AIGC detectors as decision-support tools together with provenance metadata, human review, and transparent uncertainty reporting, rather than as the sole basis for high-stakes judgments.